Received: 11 April 2022 | Accepted: 26 September 2022

DOI: 10.1111/gcb.16502

Global Change Biology WILEY

RESEARCH ARTICLE

Radiation-constrained boundaries cause nonuniform responses of the carbon uptake phenology to climatic warming in the Northern Hemisphere

Adrià Descals[1,2] | Aleixandre Verger[1,2,3] | Gaofei Yin[1,2,4] | Iolanda Filella[1,2] | Yongshuo H. Fu[5] | Shilong Piao[6] | Ivan A. Janssens[7] | Josep Peñuelas[1,2]

[1]CREAF, Cerdanyola del Vallès, Barcelona, Spain

[2]CSIC, Global Ecology Unit CREAF-CSIC-UAB, Barcelona, Spain

[3]CIDE, CSIC-UV-GV, València, Spain

[4]Faculty of Geosciences and Environmental Engineering, Southwest Jiaotong University, Chengdu, China

[5]College of Water Sciences, Beijing Normal University, Beijing, China

[6]College of Urban and Environmental Sciences, Peking University, Beijing, China

[7]Department of Biology, University of Antwerp, Wilrijk, Belgium

Correspondence
Adrià Descals, CREAF, Cerdanyola del Vallès, Barcelona 08193, Catalonia, Spain.
Email: a.descals@creaf.uab.cat

Funding information
Catalan Government, Grant/Award Number: AGAUR-2020PANDE00117 and SGR 2017-1005; CSIC Thematic Interdisciplinary Platform Teledetección, Grant/Award Number: PTI-TELEDETECT; European Research Council Synergy project, Grant/Award Number: SyG-2013-610028; Fundación Ramon Areces, Grant/Award Number: ELEMENTAL-CLIMATE; National Funds of China for Distinguished Young Scholar, Grant/Award Number: 42025101; Spanish Government, Grant/Award Number: PID2019-110521GB-I00

Abstract

Climatic warming has lengthened the photosynthetically active season in recent decades, thus affecting the functioning and biogeochemistry of ecosystems, the global carbon cycle and climate. Temperature response of carbon uptake phenology varies spatially and temporally, even within species, and daily total intensity of radiation may play a role. We empirically modelled the thresholds of temperature and radiation under which daily carbon uptake is constrained in the temperate and cold regions of the Northern Hemisphere, which include temperate forests, boreal forests, alpine and tundra biomes. The two-dimensionality of the temperature-radiation constraint was reduced to one single variable, θ, which represents the angle in a polar coordinate system for the temperature-radiation observations during the start and end of the growing season. We found that radiation will constrain the trend towards longer growing seasons with future warming but differently during the start and end of season and depending on the biome type and region. We revealed that radiation is a major factor limiting photosynthetic activity that constrains the phenology response to temperature during the end-of-season. In contrast, the start of the carbon uptake is overall highly sensitive to temperature but not constrained by radiation at the hemispheric scale. This study thus revealed that while at the end-of-season the phenology response to warming is constrained at the hemispheric scale, at the start-of-season the advance of spring onset may continue, even if it is at a slower pace.

KEYWORDS
carbon uptake phenology, climatic warming, phenology modelling, photosynthetically growing season, radiation constraints, vegetation phenology

1 | INTRODUCTION

Seasonal changes in weather conditions drive the timing of the start and end of vegetation growth (Piao et al., 2019). With recent climatic warming, the growing season has lengthened, with the start of the growing season advancing more than the end of the growing season delaying (Menzel et al., 2006; Peñuelas & Filella, 2001). Vegetation phenology influences the carbon and water cycle (Keenan et al., 2014;

Myneni et al., 1997; Richardson et al., 2010), successional transition (Chuine, 2010) and plays a role in the feedback between vegetation and climate (Peñuelas & Filella, 2009; Richardson et al., 2013). The warming-induced lengthening of the growing season has increased the carbon uptake (Le Quéré et al., 2009), offsetting atmospheric carbon from human emissions. However, how phenology may respond to future warming and whether vegetation will increase carbon sequestration remains unclear (Piao et al., 2019), which adds uncertainty to future atmospheric carbon concentration and, thus, climate projections.

Winter chilling, forcing requirements, and photoperiod trigger the start of foliar phenology (Richardson et al., 2013). Previous research suggests that chilling requirements will constrain the advance of leaf unfolding in deciduous forests by reducing temperature sensitivity (Fu et al., 2015), whereas other factors such as precipitation (Peaucelle et al., 2019) and photoperiod (Körner & Basler, 2010; Meng et al., 2021; Zohner et al., 2016) may increase the heat requirements during the ecodormancy stage and, as a result, slow down the warming-induced advance of the leaf unfolding. With regards to leaf senescence, a recent study found that increased productivity during the growing season counteracts the warming-induced delay in leaf senescence (Zani et al., 2020). These findings are based on the study of leaf phenophases in deciduous forests obtained from in situ observations (Templ et al., 2018) or remotely-sensed vegetation greenness indices (Julien & Sobrino, 2009), such as the normalized vegetation difference index (NDVI).

The key conceptual framework in these studies is that conditions preceding the phenological dates affect the timing of tree phenophases (Chuine et al., 2013). Phenology modelling has largely accounted for chilling and forcing requirements in decisuous forests (Fu et al., 2020). However, the start and end of the photosynthetically active season are directly influenced by current meteorological conditions, not by conditions preceding the phenological dates. This is evidenced by a decoupling between remotely sensed vegetation greenness and proxies of photosynthetic activity (Jeong et al., 2017; Yin et al., 2020; Zhang, Commane, et al., 2020), which indicates that vegetation might present leaves but these are not photosynthetically active because meteorological conditions are restricting photosynthetic activity at the moment. For instance, vegetation productivity declines in agreement with the decrease in radiation intensity during autumn (Zhang, Commane, et al., 2020), and a lack of available light may, thus, prompt the end of the growing season. Similarly, water availability determines the start and end of the photosynthetically active season in tropical dryland ecosystems (Eamus & Prior, 2001; Jiao et al., 2021; Zhang, Parazoo, et al., 2020).

Given the link between photosynthesis and current meteorological conditions, the seasonality of carbon uptake can be modelled with meteorological variables, and the start and end of the growing season can be determined by constraint functions (Jolly et al., 2005). The constraint functions define the photosynthesis-inhibiting thresholds that restrict the carbon uptake during the growing season. Using this phenology modelling framework, carbon uptake phenology can be, thus, determined by the most limiting factor (Zhang, Parazoo, et al., 2020). The start and end of the season occur when a limiting factor, such as air temperature and radiation intensity exceeds the threshold under which photosynthesis is constrained.

One limiting factor of the phenology of photosynthesis is the low light availability (Zhang, Commane, et al., 2020). Photosynthetic activity as a function of radiation, with constant temperature and soil water content conditions, is equivalent to light-response curves (Herrmann et al., 2020), which represent the restrictions of photosynthetic activity by low levels of radiation, even if temperature, soil water content, and other factors influencing photosynthesis are favourable. The restriction is due to the inoperability of chloroplasts and light-dependent reactions in the absence of photosynthetically active radiation (Johnson et al., 2008).

Here, we aimed to clarify the role of temperature and radiation constraints during the start and end of the photosynthetically active season and how these constraints change among ecosystems and over space. To achieve this, we proposed a phenology model based on the law of limiting factors that predicts the start and end of the photosynthetically growing season. We evaluated the current temperature and radiation constraints on the phenology of temperate and cold regions of the Northern Hemisphere, where temperature and radiation mostly regulated the vegetation phenology (Piao et al., 2019). Lastly, we estimated the potential lengthening of the growing season in a warming scenario in which radiation might take over the role as a limiting factor of photosynthetic activity phenology.

2 | MATERIALS AND METHODS

2.1 | Data

We used daily in situ records from 63 sites of the FLUXNET2015 Tier 1 data set (Pastorello et al., 2020) (see Figure S1 for the locations of the sites). The biome types at the FLUXNET sites were characterized using the MODIS MCD12Q1 V6 product (Friedl & Sulla-Menashe, 2015) for the mode of land cover during 2001–2019 and the RESOLVE Ecoregions 2017 map (Dinerstein et al., 2017). We selected the sites with at least 4 years of record and categorized as deciduous broadleaved forests (DBF; 12 sites), evergreen needleleaved forests (ENF; 25 sites), mixed forests (MX; 7 sites), and grasslands and wetlands (GRA and WET; 19 sites) in the tundra, boreal, and temperate biomes of the Northern Hemisphere according to the RESOLVE Ecoregions 2017 map. These FLUXNET sites represent 643 site-years and are located >30° N. The sites cover different range of years from 1991 to 2014. We used daily gap-filled GPP reference from GPP versions using model efficiency (MEF) and obtained from the day-time partitioning method (Pastorello et al., 2020).

For the climatic data, we used daily averages of air temperature and incoming shortwave radiation at 0.1 arc degrees from the ERA5-Land hourly data (Muñoz-Sabater et al., 2021). The phenology dates were extracted from the 4-day clear-sky daily contiguous solar-induced chlorophyll fluorescence (SIF) estimates at 0.05° from the

OCO-2 (Orbiting Carbon Observatory-2) (Zhang et al., 2018) in temperate and cold regions of the Northern Hemisphere for the 2001–2020 period. SIF observations have been demonstrated to track the seasonality of GPP globally (Sun et al., 2017). The temperate and cold regions include tundra, boreal forests, temperate broadleaf and mixed forests, and temperate coniferous forests in the RESOLVE Ecoregions 2017 map (Figure S1).

2.2 | Phenology extraction

We estimated the Start of Season (SoS) and End of Season (EoS) using the maximum-separation method (Descals et al., 2020). The maximum-separation method is a threshold-based method that can effectively estimate phenological metrics without the need of time series pre-processing, which tends to distort the seasonality of the time series. The algorithm first runs a moving window that calculates the proportion of observations that are above a given threshold *th* before the central day of the moving window (p_{before}) and after the central day (p_{after}). A moving window greater than 90 days and lower than the length of the growing season is advised for the method to be effective (Descals et al., 2020). In this study, the length of the moving window was 120 days. Then, the algorithm computes the difference between the proportions (p_{before} - p_{after}) for each day of year in the time series. The SoS is calculated as the date when the difference in proportions (p_{before} - p_{after}) reaches a minimum, and the EoS is calculated as the date when the difference is maximal. The method was used to extract the SoS and EoS from the FLUXNET GPP time series and in the climate-constraint model and growing-season index. In this study, we used a dynamic threshold for the extraction of SoS and EoS from the FLUXNET GPP and the growing-season index. The dynamic threshold *th* is computed as a percentage of the amplitude (Equation 1):

$$th = \left(I_{max} - I_{min}\right) \times P + I_{min} \quad (1)$$

The I_{max} *and* I_{min} are the maximum and minimum values of the time series (e.g. FLUXNET GPP or the growing-season index). The parameter *P* ranges from 0 to 1. We set *P* equal to 0.2, which represents a percentage of 20% of the amplitude. This low percentage ensures the reliable detection of the first and last stages of the SoS and EoS. The maximum-separation method can be applied to binary time series, which is the case of the climate-constraint model (See Section 2.4. *Climate-constraint model*). In a binary time series in which values are 0 or 1, the SoS and EoS would be the same for any percentage *P* greater than 0 and lower than 1. For this reason, we used a constant threshold *th* equal to 0.5 for the climate-constraint model.

2.3 | Phenology modelling

We proposed a phenology model that incorporates the constraints of temperature and radiation on the vegetation productivity. The model first generates a binary time series where daily observations are categorized as 0 (vegetation productivity is inhibited or constrained) and 1 (vegetation productivity is active or unconstrained by temperature and radiation). In the second step of the model, the start and end of season dates are extracted from the binary time series using the maximum-separation method. We named the model as climate-constraint model because climate time series are used to generate a binary time series of constrained and unconstrained daily observations. The binary time series is analogous to the growing-season index (Jolly et al., 2005), which is generated from cut-off functions from daily temperature, daylength, and vapor-pressure deficit (VPD), and ranges from 0 and 1 (0 = vegetation is constrained and 1 = vegetation is unconstrained).

The modelled SoS and EoS were compared with estimated SoS and EoS extracted from in situ GPP time series at the FLUXNET sites. The performance of the model was evaluated in terms of root-mean-squared-error (RMSE). As the growing-season index, the climate-constrained model assumes no forcing requirements for the SoS and EoS; the growing season starts as soon as climate conditions are favorable for vegetation growth, respectively. To test this assumption, we compared the performance of the climate-constrained model with the photo-threshold model (Meng et al., 2021), a model based on the growing-degree-day model. We also compared the performance of the SoS and EoS extracted from the growing-season index.

2.4 | Climate-constraint model

The approach for phenological modelling categorizes daily time series of temperature *T(t)* (°C) and incoming shortwave radiation *R(t)* (W m^{-2}) into a binary time series *B(t)* with values 0 (constrained) and 1 (unconstrained). The classification was done with a threshold function (Equation 2); vegetation was considered unconstrained when daily temperature and radiation were above the threshold function. The threshold function has the form of a rational function with one asymptote for temperature (T_{thresh}) and another for radiation (R_{thresh}) (Figure 1a). The curvature of the rational function is defined by parameter *C* (unitless). The parameter *C* in Equation (2) reflects the covariation of temperature and radiation constraints. Instead of a constant threshold for temperature and radiation, the parameter *C* reflects the curvature of the threshold function and provides a threshold that depends on the levels of temperature and light availability (i.e., high levels of temperature reduce the radiation constraint). We used a rational function owing to the relationship of FLUXNET GPP with air temperature and shortwave radiation (Figure 1b).

$$B(t) = \begin{cases} 1 & \frac{C}{T(t) - T_{thresh}} + R_{thresh} - R(t) < 0 \\ 0 & \frac{C}{T(t) - T_{thresh}} + R_{thresh} - R(t) \geq 0 \\ 0 & T(t) < T_{thresh} \end{cases} \quad (2)$$

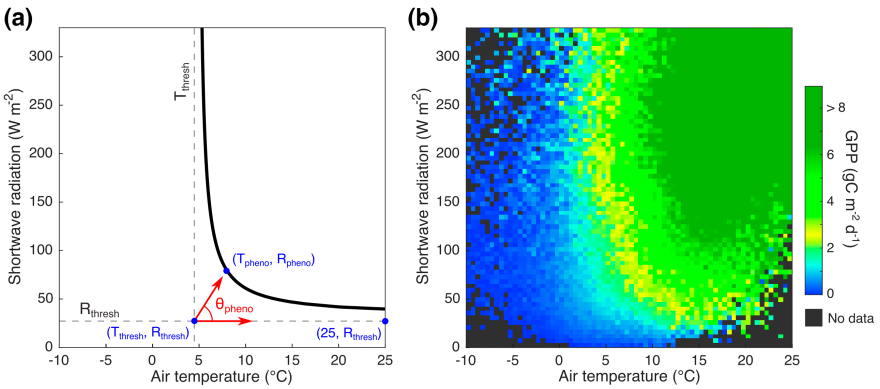

FIGURE 1 Graphical representation of the calculation of parameters in the climate-constraint model. (a) Graphical representation of the threshold function (black line) and the angle θ. The threshold function consists of a rational function defined by the asymptotes in T_{thresh} and R_{thersh}. The angle θ_{pheno} represents the radiation constraint of temperature and radiation during a phenological event. (b) Mean gross primary production (GPP) as a function of air temperature and incoming shortwave radiation for all observations of the FLUXNET sites in the cold and temperate regions of the Northern Hemisphere.

The time series of FLUXNET GPP and ERA5-Land air temperature and shortwave radiation were used to calibrate the parameters T_{thresh}, R_{thresh}, and C. To accomplish this, the FLUXNET GPP was converted to a binary time series: 0 when GPP was < GPP_{thresh} and 1 when GPP was > GPP_{thresh} C m^{-2} d^{-1}. We used a GPP_{thresh} equal to 2 C m^{-2} d^{-1}, which is approximately the median GPP of the 192,709 observations and represents a low GPP threshold that ensure the first and last stages of the SoS and EoS, respectively. The calibration was done using the simplex search method (Lagarias et al., 1998).

The second step of the model consists of the extraction of phenological dates (SoS and EoS) from the binary time series *B(t)* using the maximum-separation method (Descals et al., 2020). The binary time series *B(t)* reflects that vegetation is unconstrained whenever temperature and radiation conditions are favorable for vegetation growth. Thus, the binary time series may reflect unconstrained observations when sporadic favorable conditions occur during the dormant period, and the SoS could incorrectly identified in such scenario. To avoid this shortcoming, Jolly et al. (2005) proposed a 21-day moving average of the growing-season index to remove extreme events that can prematurely detect the start of the growing season. In this study, we used the maximum-separation method because the method detects the SoS only when there are many values that are unconstrained after the dormant period. Similarly, the EoS is detected when there is a substantial decline in the number of unconstrained observations after the growing season. Thus, the daily observations of favorable temperature and radiation that may occur sporadically during the dormant period are not detected as SoS or EoS by the maximum-separation method.

2.5 | Growing-season index

The growing-season index was designed to reproduce the NDVI time series from air temperature, daylength, and VPD (Jolly et al., 2005). The growing-season index is calculated from cut-off functions for temperature (Equation 3; in °C), daylength (Equation 4; in hours), and VPD (Equation 5, in kPa), which bound the climate time series to values between 0 and 1. The cut-off functions are defined by a minimum and a maximum threshold for temperature (T_{min} and T_{max}), daylength (DL_{min} and DL_{max}), and VPD (VPD_{min} and VPD_{max}). The growing-season index is the multiplication of T_{gsi}, DL_{gsi}, and VPD_{gsi} (Equation 6) and ranges from 0 (vegetation is fully constrained) to 1 (vegetation is fully unconstrained).

$$T_{gsi}(t) = \begin{cases} 0 & T(t) \le T_{min} \\ \dfrac{T(t) - T_{min}}{T_{max} - T_{min}} & T_{min} < T(t) < T_{max} \\ 1 & T(t) \ge T_{max} \end{cases} \quad (3)$$

$$DL_{gsi}(t) = \begin{cases} 0 & DL(t) \le DL_{min} \\ \dfrac{DL(t) - DL_{min}}{DL_{max} - DL_{min}} & DL_{min} < DL(t) < DL_{max} \\ 1 & DL(t) \ge DL_{max} \end{cases} \quad (4)$$

$$VPD_{gsi}(t) = \begin{cases} 0 & VPD(t) \le VPD_{min} \\ \dfrac{VPD(t) - VPD_{min}}{VPD_{max} - VPD_{min}} & VPD_{min} < VPD(t) < VPD_{max} \\ 1 & VPD(t) \ge VPD_{max} \end{cases} \quad (5)$$

$$GSI(t) = T_{gsi}(t) \times DL_{gsi}(t) \times VPD_{gsi}(t) \quad (6)$$

Equation (3) originally used daily minimum air temperature but, for consistency with the climate-constrained function, we used daily mean air temperature. The daylength was calculated as a function of time (day of the year) and latitude (°) using the model proposed in (Forsythe et al., 1995). VPD was calculated using the formula in Yuan et al. (2019), which uses air and dew point temperature, both variables included in the ERA5-Land dataset. Jolly et al. (2005) defined the threshold

parameters of the cut-off functions. However, we calibrated these parameters for our case study because (1) we used different climate data, (2) we used mean air temperature instead of minimum air temperature, and (3) we aimed to reproduce the FLUXNET GPP, representing vegetation productivity, instead of the NDVI, which is an indicator of green biomass. The calibration of the parameters was done using the simplex search method.

The growing-season index can be used as a phenology model. As the climate-constrained model, phenological dates can be extracted from the growing-season index. We used the maximum-separation method and a dynamic threshold of 20% of the amplitude to determine the SoS and EoS dates.

2.6 | Photo-threshold model

The photo-threshold works similarly as the growing-degree-day model (Hänninen, 2016) but replaces the arbitrary date when forcing starts accumulating (generally January 1) with the date when daylength reaches the threshold DL_{start} (Meng et al., 2021). The state of forcing *Sf(t)* (Equation 7) is calculated as the summation of the rate of forcing *Rf(t)* starting from DL_{start} (Equation 8). Temperature *T(t)* is offset with a base temperature T_{base} (0°C in this study). The SoS occurs the date when the state of forcing *Sf(t)* is higher than the forcing requirement *F*. If the forcing requirement is not met, the model forces the SoS to the first day of year when daylength surpasses DL_{end}. In the photo-threshold model, DL_{start}, DL_{end}, and *F* are the parameters to calibrate. The simplex search method was used for the calibration.

$$Sf(t) = \sum_{t_0} Rf(T(t)) \tag{7}$$

$$Rf(t) = \begin{cases} (t) - T_{base} & T(t) > T_{base} \\ 0 & T(t) \leq T_{base} \end{cases} \tag{8}$$

2.7 | Estimation of temperature and radiation constraints on phenological dates

To quantify the limitations of radiation and temperature on the start and end of the growing season, we reduced the two-dimensionality of the temperature-radiation constraint to one single variable; θ. The angle θ was calculated geometrically (Equation 9) based on the threshold function (Equation 2) and given the points Pa, Pb, and Pc, where Pa and Pb have fixed coordinates in (T_{thresh}, R_{thresh}) and (25, R_{thresh}), respectively. The coordinates of Pc are given by the temperature and shortwave radiation at the time of the phenological event (T_{pheno} and R_{pheno}). We calculated T_{pheno} and R_{pheno} as the mean temperature and radiation 7 days before and after the phenological event (SoS and EoS) to avoid noisy values of θ due to variation on daily temperature and radiation. A graphical representation of the calculation of θ is shown in Figure 1a. The temperature values (T_{pheno} and T_{thresh}) were scaled by dividing by 25°C, and radiation values (R_{pheno} and R_{thresh}) were scaled by dividing by 300 W m^{-2}. These scaling values represent approximately the 95th percentile of all temperature and radiation observations in the FLUXNET sites.

$$\theta = \tan^{-1}\left(\frac{25(R_{pheno} - R_{thresh})}{350(T_{pheno} - T_{thresh})}\right) \tag{9}$$

A high temperature and low amount of radiation at the time of the phenological event lead to low values of θ proximal to 0°, and a low temperature and high amount of radiation at the time of the phenological event lead to high values of θ proximal to 90°. Values of θ <0 or>90° were clamped to 0 and 90°, respectively.

2.8 | Estimation of the potential lengthening of the growing season

We converted the current climate constraints on phenology into potential lengthening of the growing season. The potential SoS and EoS (SoS_{pot} and EoS_{pot}) represent the dates under a warming scenario in which SoS and EoS would be restricted only by radiation. This gives a practical quantification of the climate constraints on the phenological dates. For instance, a small difference between EoS and EoS_{pot} indicates that future warming will not delay the EoS. For the calculation of SoS_{pot} and EoS_{pot}, we changed the threshold function in Equation 2 to a constant radiation threshold equal to R_{thresh}. The observation was considered inhibited when shortwave radiation was <R_{thresh} and active when it was >R_{thresh}. Analytically, this would correspond to the climate-constraint function (Equation 2) having a high temperature *T(t)* that is nearly infinity.

2.9 | Estimation of temperature dependency

The dependency of SoS and EoS on temperature was estimated for 2001–2020 using ERA5-Land and the phenological dates extracted from the SIF time series. The SoS and EoS were extracted using a dynamic threshold of 20% the amplitude. The mean air temperature during the phenological dates were calculated as the average daily air temperature during ±7 days the SoS and EoS. Temperature dependency was estimated using the coefficient of correlation between temperature and phenological dates obtained from SIF time series, which provides more spatial and temporal coverage (2001–2020) than the FLUXNET GPP records. We used Pearson correlations, which is termed temperature dependency, instead of the conventional metric of temperature sensitivity (Fu et al., 2015) because the latter overestimates the sensitivity when the temperature time series is highly variable (Keenan et al., 2020), which could potentially weaken the spatial analysis in our study. Pixels were masked if minimum winter radiation was below R_{thresh}; latitudes where winter radiation is above R_{thresh} are potentially not limited by radiation and present SIF values greater than 0. The minimum winter radiation

was estimated as the average shortwave radiation from day of year 345 to 365 and aggregated over the 2001–2020 period.

3 | RESULTS

The parameters T_{thresh}, R_{thresh}, and C, which define the threshold function of temperature and radiation, were 2.56°C, 26.5 W m^{-2}, and 342 when considering all FLUXNET site-years (Table 1). The parameters T_{thresh} and R_{thresh}, which define the asymptotes of the rational function, did not change substantially among vegetation types; ENF presented the lowest T_{thresh} (2.07°C) and highest R_{thresh} (34.8 W m^{-2}), while DBF presented the highest T_{thresh} (2.71°C) and lowest R_{thresh} (25.9 W m^{-2}). Temperature and radiation during the FLUXNET GPP SoS and EoS occurred closely to the threshold function in ENF and MX (Figure S2).

The SoS and EoS were modeled using climatic time series and then compared to the observed SoS and EoS in the FLUXNET sites. The estimated and observed phenological metrics showed the highest agreement in ENF (RMSE was 11.78 d and 12.97 d for SoS and EoS, respectively) (Figure 2). The model output agreed well with observed SoS and EoS in ENF sites, despite the wide range of latitudes and various biome type; constraints of temperature and radiation explained the SoS and EoS in the FLUXNET site San Rossore (IT-SRo), with a Mediterranean climate, as well as the FLUXNET site Saskatchewan (Ca-Obs), covering a boreal forest. The largest RMSE was found for SoS in deciduous forests (34.38 d), which presented a large bias for the SoS (ME was 34.4 d in DBF compared to the 0.4 d in ENF).

Model parameters in the growing-season index and the photo-threshold model were overall similar. However, the forcing requirement F, in the photo-threshold model, was a parameter that differed substantially among vegetation types (Table 1). The forcing requirement F ranged from 35.7°C in ENF to 258.4°C in DBF. The photo-threshold method presented the highest RMSE in DBF and GRA (Table 2) but, in ENF and MX, the RMSE was similar to the climate-constraint function. The SoS and EoS modeled using the growing-season index showed a higher RMSE compared with the climate-constraint model in all vegetation types.

Temperature and radiation during SoS and EoS at the FLUXNET sites were within the ranges defined by the threshold function in ENF and MX (Figure S2), although on average the daily mean radiation differed between SoS (air temperature, 7.5°C; shortwave radiation, 212 W m^{-2}) and EoS (air temperature, 7.7°C; shortwave radiation, 94 W m^{-2}) in all vegetation types, which suggests a contrasting limitation of temperature and radiation during the SoS and EoS in temperate and cold regions of the Northern Hemisphere. Values of θ, extracted from SIF time series, were on average high during the SoS for 2001–2020 in the cold and temperate regions of the Northern Hemisphere (median and 5–95th percentile range was 87 [65, 98]), which contrasted with the low θ during the EoS (32 [14, 50]) (Figure 3a). Specifically, the regions where radiation limitation was highest during the SoS and EoS correspond to temperate Europe (Figure S3), while temperature restricted the SoS and EoS in high-latitude and high-altitude regions.

The limitation of radiation to photosynthesis was linked to a low sensitivity of phenology to temperature in temperate and cold regions of the Northern Hemisphere. SoS was on average more dependent than EoS to temperature. The dependency of phenological dates to temperature was significantly lower when the limitation of radiation was high (Figure 4). Regions with the highest radiation limitation during the SoS, where values of θ were lower than the 5th percentile ($\theta < 65$), presented a significantly lower temperature dependency ($R = -0.50$) than the rest of the regions ($R = -0.63$). Similarly, regions with the lowest radiation limitation during the EoS, defined as values greater than the 95th percentile ($\theta > 50$), exhibited a significantly greater temperature dependency ($R = 0.23$) than the rest of the regions ($R = 0.16$).

Lastly, we defined the dates when radiation could potentially become the climatic variable that fully restricted photosynthetic activity during spring onset and autumnal senescence as SoS_{pot} and EoS_{pot}, representing the days of the year when daily shortwave radiation reaches threshold R_{thresh} (27 W m^{-2}) in spring and autumn. The 27 W m^{-2} threshold represents the radiation threshold if temperature did not constrain photosynthesis. The estimated EoS was generally similar to the EoS_{pot} based on the FLUXNET and gridded climatic data (Figures 3b and 5). The mean difference EoS_{pot} – EoS was 23.6 d in the FLUXNET sites. The observed SoS estimated using FLUXNET and gridded climatic data, in contrast, was far from reaching SoS_{pot} at the hemispheric scale

TABLE 1 Parameters of the climate-constraint model, growing-season index, and the photo-threshold model

	Climate-constraint model			Growing-season index						Photo-threshold model		
	T_{thresh}	R_{thresh}	C	T_{min}	T_{max}	DL_{min}	DL_{max}	VPD_{min}	VPD_{max}	DL_{start}	DL_{end}	F
ALL	2.56	26.52	342.2	−1.57	4.33	13.1	13.7	0.88	4.18	12.6	22.1	73.9
ENF	2.07	34.83	112.4	−1.84	4.75	12.0	12.6	0.71	3.85	11.4	21.5	35.7
DBF	2.71	25.90	338.1	−1.99	4.92	10.2	11.2	0.91	4.30	12.6	22.1	258.4
MX	2.50	27.00	350.0	−1.49	4.92	12.1	13.0	0.67	3.75	11.3	14.6	118.8
GRA	2.56	27.30	367.8	−2.01	5.23	10.2	11.4	0.83	4.14	12.6	19.0	95.0

Note: The parameters were calibrated using an optimization algorithm that found the lowest RMSE between modeled and estimated phenological dates at the FLUXNET sites.

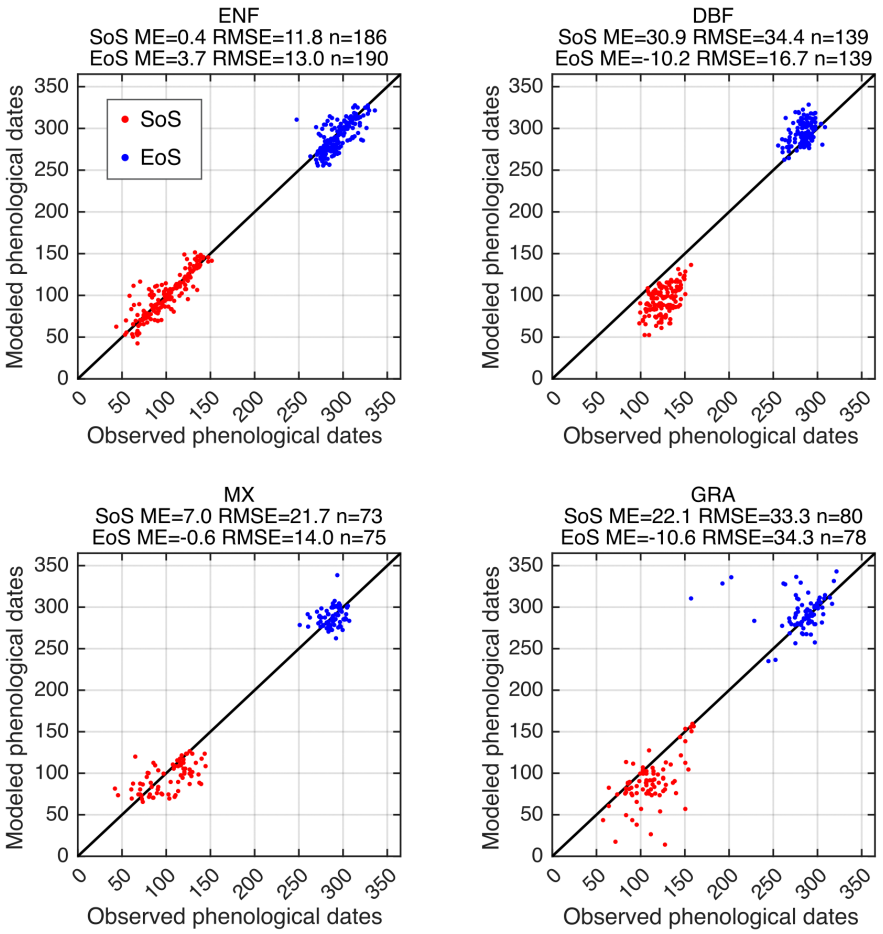

FIGURE 2 Comparison between observed and simulated start of the growing season (SoS) (in red) and end of the growing season (EoS) (in blue) at the FLUXNET towers in evergreen needleleaved forests (ENF), deciduous broadleaved forests (DBF), mixed forests (MX), and grasslands (GRA). Observed SoS and EoS were obtained from GPP time series from the FLUXNET towers. Simulated SoS and EoS were obtained from ERA5-Land temperature and radiation time series using the climate-constrained model. The titles of the charts report the mean error (ME), the root-mean-squared-error (RMSE), and the number of observations (*n*).

TABLE 2 Root-mean-squared error (RMSE) between modeled and estimated phenological dates at the FLUXNET sites

	RMSE (start of season)			RMSE (end of season)	
	Climate-constraint model	Growing-season index	Photo-threshold model	Climate-constraint model	Growing-season index
ALL	27.22	21.12	22.35	21.72	50.93
ENF	11.78	10.74	16.04	12.97	31.11
DBF	34.38	9.16	58.69	16.71	28.54
MX	21.74	17.87	23.26	13.97	43.12
GRA	33.26	18.70	48.44	34.33	45.85

(mean difference SoS_{pot} – SoS was –79.3 d for FLUXNET). SoS was only close to SoS_{pot} in Europe.

4 | DISCUSSION

Our results indicate that the photosynthetically growing season begins shortly after conditions for growth become favorable and ceases when these conditions decline in evergreen needleaved forests. Climate constraint boundaries, which define the threshold under which photosynthesis is inhibited, can differentiate between active and restricted vegetation stages (Jolly et al., 2005; Zhang, Parazoo, et al., 2020) and, thus, determine the phenological dates across latitudes. Our findings highlight the necessity of considering radiation, temperature, and their covariance in modelling the photosynthetically active season in evergreen needleleaved forests and their responses to climatic warming. The results did not prove that limiting factors determine the start and end of the growing season in other vegetation types other than evergreen needleaved forests. The climate-constraint model is not suited for modelling the spring onset in deciduous forests, which require heat accumulation (Richardson et al., 2013) and, in certain deciduous species, chilling requirements (Hänninen, 2016) for bud development and leaf unfolding.

Our results highlight that temperature and radiation constraints differ spatially during the SoS and EoS, indicating that vegetation will respond to climate change differently depending on the region of the Northern Hemisphere. Radiation is already constraining the SoS and EoS in regions such as Europe, while the EoS is largely constrained by radiation in the Northern Hemisphere, as indicated previously (Zhang, Commane, et al., 2020), but not in highly elevated areas where temperature mainly limit photosynthesis in autumn. Moreover, the advance of spring onset was overall not limited by radiation, and future warming can potentially lead to an advance of the spring onset of carbon uptake in evergreen needleaved forests, which respond promptly to favorable temperature and radiation conditions.

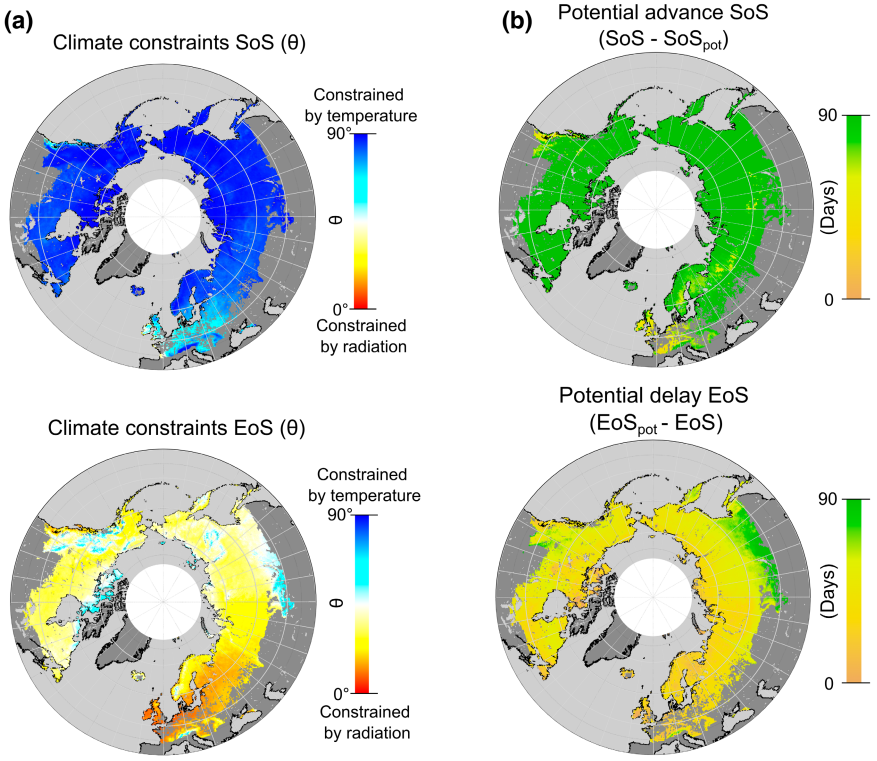

FIGURE 3 Potential lengthening of the growing season in temperate and cold regions of the Northern Hemisphere. (a) Magnitudes of the constraints on the start and end of season (SoS and EoS) by radiation and temperature. The temperature constraints increase with θ, and the radiation constraint decreases with θ. (b) Potential advance of the SoS (SoS − SoS$_{pot}$) and potential delay of the EoS (EoS − EoS$_{pot}$). SoS$_{pot}$ and EoS$_{pot}$ represent the start and end of the growing season if radiation was the only limiting factor. SoS and EoS were estimated using the OCO-2 SIF data set and temperature and radiation were extracted from the ERA5-Land for 2001–2020.

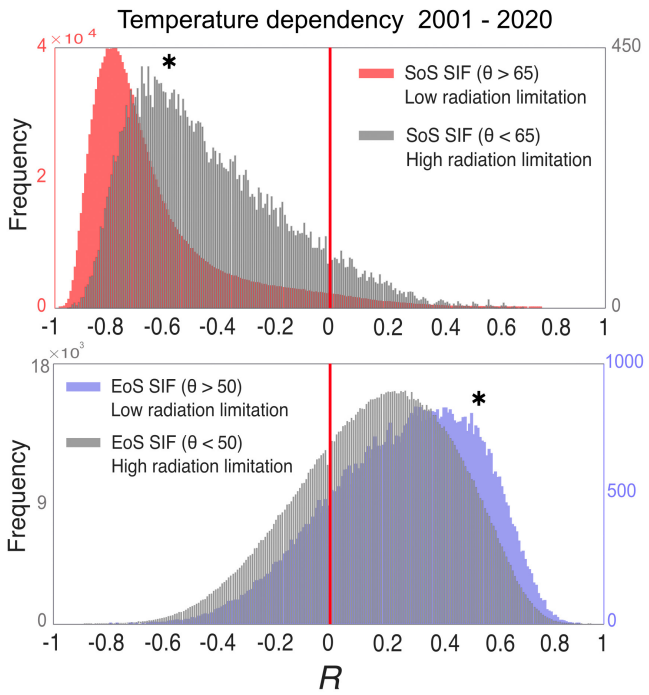

FIGURE 4 Histograms of the coefficients (R) for the correlation between temperature (ERA5-Land) and phenological dates (estimated from the OCO-2 SIF time series) during 2001–2020. The asterisk represents that mean R was significantly different in the regions with the highest radiation constrain during the SoS ($\theta < 65$) and in the regions with the highest temperature constrain during the EoS ($\theta > 50$). The threshold of θ for the SoS represents the 5th percentile of all mean θ values and the threshold of θ for the EoS is the 95th percentile of the mean θ values for the 2001–2020 period.

The climate-constraint model is similar to the growing-season index, which considers three separate cut-off functions for temperature, daylength, and VPD (Jolly et al., 2005). A difference between these models is that the climate-constraint model considers the interaction between the constraints of radiation and temperature, which might explain the better estimates of phenological dates. Our model used radiation instead of daylength. Daylength has been proposed as a factor controlling the spring onset (Körner & Basler, 2010) and leaf senescence (Way & Montgomery, 2015). Daylength also plays a role in regulating the forcing requirements in deciduous forests (Meng et al., 2021). However, radiation is more suited for modelling the start and end of the photosynthetically active season (Zhang, Commane, et al., 2020), primarily because photosynthesis is directly linked to light availability (Herrmann et al., 2020).

The cold-avoidance strategy of deciduous forests may explain their exception to the law of the limiting factors in the phenology of the carbon uptake, as revelead by the long difference between modelled SoS and flux-based SoS in deciduous forests. Deciduous trees respond differently than evergreen conifers to cold winters. Most conifers in temperate and cold regions have a cold-tolerant strategy. Leaves in conifers resist cold, reject excessive radiation when temperatures are still low in the spring, and resume photosynthetic activity as soon as climatic conditions are favorable (Chang et al., 2021). In contrast, deciduous trees shed their leaves in autumn and leaf budbreak in spring (Chuine et al., 2013). This would account for our findings that deciduous trees remain dormant during spring, even when photosynthesis conditions are favorable. Such strategy would also avoid leafing out prematurely to prevent frost damage

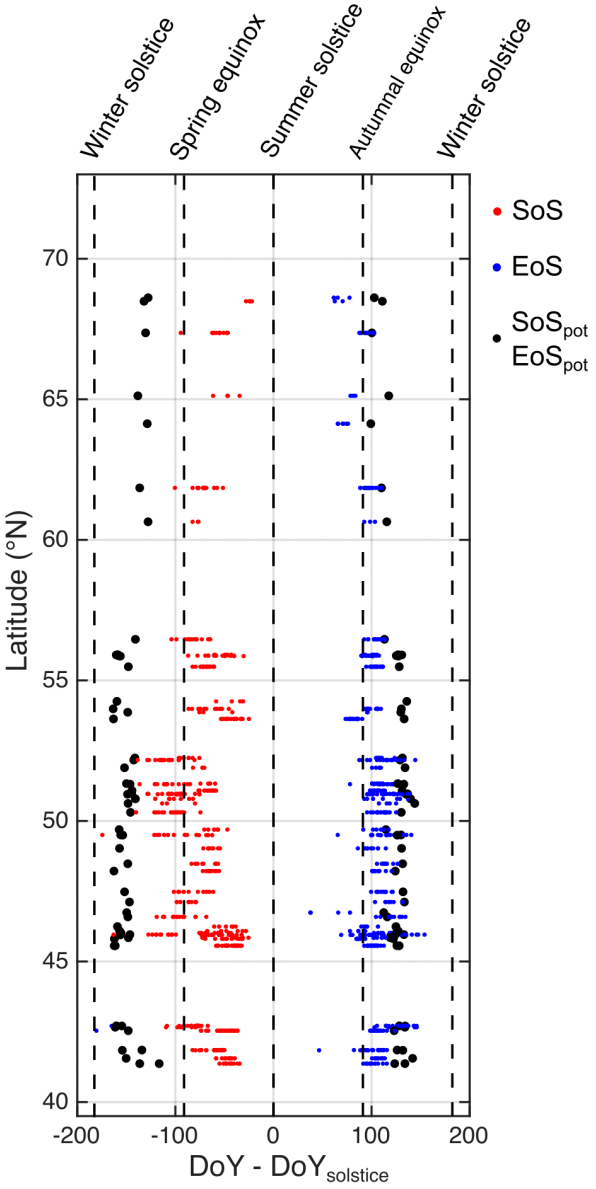

FIGURE 5 Potential lengthening of the growing season in the FLUXNET sites. *Y*-axis show the latitudinal gradients of the observed start of season (SoS; red dots) and the End of Season (EoS; blue dots) obtained from the GPP time series at the FLUXNET towers. The mean potential start of season SoS_{pot} and end of season EoS_{pot} (black dots) represent the Day of Year (DoY) when shortwave radiation surpasses the 27 W m^{-2} threshold. The DoY was offset such that the summer solstice ($DoY_{solstice}$) is the origin of the axis.

(Meng et al., 2021). The ecodormancy stage is only broken when a certain amount of heat is accumulated (Richardson et al., 2013).

Temperature was the main limiting factor during spring onset, but temperature and radiation have been limiting during autumn in temperate and cold regions of the Northern Hemisphere (Zhang, Commane, et al., 2020). Temperature is seasonally asymmetrical, with lower temperatures before the summer solstice than after. That is because leafless temperate deciduous forests and snow-covered ecosystems have a high albedo in the springtime. Tundra FLUXNET sites provide key examples; daily mean air temperatures remained <2.5°C just before the summer solstice, when annual radiation was at its peak. Because spring is colder than autumn, the growing season begins closer to the summer solstice than the senescence stage does. In contrast, the small difference betwee EoS and EoS_{pot} indicates a strong constraint of radiation on GPP senescence in the Northern Hemisphere and suggests that future climatic warming cannot delay the end of the photosynthetically growing season due to low levels of radiation in autumn. During the EoS, the radiation constraint on photosynthetic activity is increased because autumn temperatures remain high. This suggests that, as a result of future warming, radiation constraints will increase further in autumn, limiting the delay of the EoS.

The strongest radiation constraint was found in temperate forest biomes in Europe, where the maritime influence kept temperatures favorable for vegetation growth in autumn. In contrast, temperature mostly constrained carbon uptake phenology in the alpine biome, which suggests that warming could potentially advance the SoS and delay the EoS in high-elevated regions more than radiation-restricted vegetation. This further support the claims of spatial homogeneity in spring phenology (Liu et al., 2019) and the reduction of the altitudinal gradient in phenological dates as a result of global warming (Vitasse et al., 2018). As found in previous studies, high-elevated vegetation will lengthen the growing season more than low-elevated vegetation with climatic warming, equalizing phenological dates across elevations.

Phenology research has had a major focus on the timing of phenophases in temperate deciduous forests (Piao et al., 2019). The PEP725, the most widely used in situ phenological database, mostly contains phenophase records of deciduous species in Central Europe (Templ et al., 2018). However, we showed that the climate of Europe has milder temperatures than other areas of the same latitude, exacerbating the limitation of radiation in both spring and autumn. Secondly, deciduous forests have high heat requirements for their release from dormancy that differ from other vegetation types (Richardson et al., 2013), which explains their different responses to favorable weather conditions during the spring onset. Lastly, the coverage of deciduous trees and mixed forests represents only 18% of the temperate and cold regions of the Northern Hemisphere (Figure S1). All these factors indicate that forecasted shifts in phenology under climatic warming and projections of carbon sequestration by vegetation, based on the sole modelling of phenophases of deciduous trees in Central Europe, cannot be scaled to other biomes of the Northern Hemisphere. Our findings highlight the importance of extensive carbon uptake observations for the study of the global carbon cycle. Carbon uptake phenology is more difficult to track than tree phenophases, and only in situ (FLUXNET) and satellite (SIF) observations have been made extensively over the last two decades (Pastorello et al., 2020; Zhang et al., 2018).

The asymmetric temperature variability over the season explains the different radiation and temperature constraints during the SoS and EoS. In turn, the different radiation and temperature constraints explain the nonuniform seasonal temperature dependency during

the SoS and EoS and across the temperate and cold regions, suggesting divergent responses of vegetation phenology to future climatic warming. The dependency of the SoS and EoS to temperature was significantly lower in regions where radiation constraints were the highest. These results indicate that the sensitivity of vegetation phenology to temperature decreases with the increasing constraints of radiation. Our results show that the senescence stage has a low temperature dependency due to the constraints of radiation, and this might be a reason for the lower magnitude in the EoS delay than the SoS advance (Menzel et al., 2006). In deciduous forests, other alternative mechanisms for leaf senescence include the growing-season productivity (Zani et al., 2020). SoS could continue its advance with future warming, even if it is at a lower pace (Fu et al., 2015), although the advance of spring onset would be highly spatially variable depending on the local radiation limitations. In needleaved forests, radiation should be taken into account when modeling how the phenology of the photosynthetically active season will change as the climate warms.

5 | CONCLUSIONS

This study showed that limiting factors determined the start and end of the photosynthetically active season in evergreen needleaved forests in temperate and cold regions of the Northern Hemisphere. Our findings showed that temperature and radiation constraints on vegetation productivity differed depending on the regions of the Northern Hemisphere. In addition, the radiation constraints were different during the SoS and EoS, indicating that carbon uptake phenology will respond to future warming differently in spring than autumn. Temperature was overall limiting photosynthesis during the spring onset, but temperature and radiation were both constraining at the end of the growing season. The radiation constraint increases in autumn because temperatures remain high at that stage of the season, suggesting that future warming will not delay the end of the photosynthetically active season. In contrast, radiation limitation was low during the spring onset and the start of the season was highly sensitive to temperature, which indicates that the photosynthetically active season could continue overall its advance with future warming. Our results highlight the importance of taking radiation, temperature, and their covariance into account when modeling the photosynthetically active season in evergreen needleleaved forests and its responses to climatic warming.

ACKNOWLEDGMENTS

The authors acknowledge the financial support from the European Research Council Synergy project SyG-2013-610028 IMBALANCE-P, the Catalan Government grants AGAUR-2020PANDE00117 and SGR 2017-1005, the Spanish Government grant PID2019-110521GB-I00, the Fundación Ramon Areces grant ELEMENTAL-CLIMATE, and the National Funds of China for Distinguished Young Scholar grant No. 42025101. This work represents a contribution to CSIC Thematic Interdisciplinary Platform Teledetección (PTI-TELEDETECT).

CONFLICT OF INTEREST

The authors declare that there is no conflict of interest.

DATA AVAILABILITY STATEMENT

The data that support the findings of the study are openly available from the FLUXNET2015 dataset at https://fluxnet.org/data/fluxnet2015-dataset/, the contiguous OCO-2 SIF at https://figshare.com/articles/dataset/CSIF/6387494, the ERA5-Land Hourly - ECMWF Climate Reanalysis at https://doi.org/10.24381/cds.e2161bac, the MODIS Land Cover Dynamics MCD12Q2v6 at https://doi.org/10.5067/MODIS/MCD12Q2.006, and the RESOLVE Ecoregions 2017 at https://doi.org/10.1093/biosci/bix014 and in Google Earth Engine at https://developers.google.com/earth-engine/datasets/catalog/RESOLVE_ECOREGIONS_2017. Furthermore, a sample python code of the climate-constraint model is available at https://github.com/adriadescals/climate_constraint_model. The code for the Maximum Separation method, which was used for the phenology extraction, can be found at https://github.com/adriadescals/MaximumSeparation_method.

ORCID

Adrià Descals https://orcid.org/0000-0003-1644-3036
Aleixandre Verger https://orcid.org/0000-0001-9374-1745
Gaofei Yin https://orcid.org/0000-0002-9828-7139
Iolanda Filella https://orcid.org/0000-0001-6262-5733
Yongshuo H. Fu https://orcid.org/0000-0002-9761-5292
Shilong Piao https://orcid.org/0000-0001-8057-2292
Ivan A. Janssens https://orcid.org/0000-0002-5705-1787
Josep Peñuelas https://orcid.org/0000-0002-7215-0150

REFERENCES

Chang, C. Y.-Y., Bräutigam, K., Hüner, N. P., & Ensminger, I. (2021). Champions of winter survival: Cold acclimation and molecular regulation of cold hardiness in evergreen conifers. *New Phytologist*, *229*(2), 675–691.

Chuine, I. (2010). Why does phenology drive species distribution? *Philosophical Transactions of the Royal Society B: Biological Sciences*, *365*(1555), 3149–3160.

Chuine, I., de Cortazar-Atauri, I. G., Kramer, K., & Hänninen, H. (2013). Plant development models. In *Phenology: An integrative environmental science* (pp. 275–293). Springer.

Descals, A., Verger, A., Yin, G., & Peñuelas, J. (2020). A threshold method for robust and fast estimation of land-surface phenology using Google Earth Engine. *IEEE Journal of Selected Topics in Applied Earth Observations and Remote Sensing*, *14*, 601–606.

Dinerstein, E., Olson, D., Joshi, A., Vynne, C., Burgess, N. D., Wikramanayake, E., Hahn, N., Palminteri, S., Hedao, P., Noss, R., Hansen, M., Locke, H., Ellis, E. C., Jones, B., Barber, C. V., Hayes, R., Kormos, C., Martin, V., Crist, E., … Saleem, M. (2017). An ecoregion-based approach to protecting half the terrestrial realm. *Bioscience*, *67*(6), 534–545.

Eamus, D., & Prior, L. (2001). Ecophysiology of trees of seasonally dry tropics: Comparisons among phenologies. In *Advances in Ecological Research* (pp. 113–197). Elsevier.

Forsythe, W. C., Rykiel, E. J., Jr., Stahl, R. S., Wu, H., & Schoolfield, R. M. (1995). A model comparison for daylength as a function of latitude and day of year. *Ecological Modelling*, *80*(1), 87–95.

Friedl, M., & Sulla-Menashe, D. (2015). MCD12Q1 MODIS/Terra+ aqua land cover type yearly L3 global 500m SIN grid V006 [data set]. *NASA EOSDIS Land Processes DAAC*, *10*, 200.

Fu, Y., Li, X., Zhou, X., Geng, X., Guo, Y., & Zhang, Y. (2020). Progress in plant phenology modeling under global climate change. *Science China Earth Sciences*, *63*(9), 1237–1247.

Fu, Y. H., Zhao, H., Piao, S., Peaucelle, M., Peng, S., Zhou, G., Ciais, P., Huang, M., Menzel, A., Peñuelas, J., Song, Y., Vitasse, Y., Zeng, Z., & Janssens, I. A. (2015). Declining global warming effects on the phenology of spring leaf unfolding. *Nature*, *526*(7571), 104–107. https://doi.org/10.1038/nature15402

Hänninen, H. (2016). The annual phenological cycle. In *Boreal and temperate trees in a changing climate* (pp. 35–138). Springer.

Herrmann, H. A., Schwartz, J.-M., & Johnson, G. N. (2020). From empirical to theoretical models of light response curves-linking photosynthetic and metabolic acclimation. *Photosynthesis Research*, *145*(1), 5–14.

Jeong, S.-J., Schimel, D., Frankenberg, C., Drewry, D. T., Fisher, J. B., Verma, M., Berry, J. A., Lee, J.-E., & Joiner, J. (2017). Application of satellite solar-induced chlorophyll fluorescence to understanding large-scale variations in vegetation phenology and function over northern high latitude forests. *Remote Sensing of Environment*, *190*, 178–187.

Jiao, W., Wang, L., Smith, W. K., Chang, Q., Wang, H., & D'Odorico, P. (2021). Observed increasing water constraint on vegetation growth over the last three decades. *Nature Communications*, *12*(1), 1–9.

Johnson, A., Alberts, B., Lewis, J., Raff, M., Roberts, K., & Walter, P. (2008). *Molecular biology of the cell, garland science*. Taylor & Francis Group.

Jolly, W. M., Nemani, R., & Running, S. W. (2005). A generalized, bioclimatic index to predict foliar phenology in response to climate. *Global Change Biology*, *11*(4), 619–632.

Julien, Y., & Sobrino, J. (2009). Global land surface phenology trends from GIMMS database. *International Journal of Remote Sensing*, *30*(13), Art. 13.

Keenan, T. F., Gray, J., Friedl, M. A., Toomey, M., Bohrer, G., Hollinger, D. Y., Munger, J. W., O'Keefe, J., Schmid, H. P., Wing, I. S., Yang, B., & Richardson, A. D. (2014). Net carbon uptake has increased through warming-induced changes in temperate forest phenology. *Nature Climate Change*, *4*(7), 598–604.

Keenan, T. F., Richardson, A. D., & Hufkens, K. (2020). On quantifying the apparent temperature sensitivity of plant phenology. *New Phytologist*, *225*(2), 1033–1040.

Körner, C., & Basler, D. (2010). Phenology under global warming. *Science*, *327*(5972), 1461–1462.

Lagarias, J. C., Reeds, J. A., Wright, M. H., & Wright, P. E. (1998). Convergence properties of the Nelder–Mead simplex method in low dimensions. *SIAM Journal on Optimization*, *9*(1), 112–147.

Le Quéré, C., Raupach, M. R., Canadell, J. G., Marland, G., Bopp, L., Ciais, P., Conway, T. J., Doney, S. C., Feely, R. A., Foster, P., Friedlingstein, P., Gurney, K., Houghton, R. A., House, J. I., Huntingford, C., Levy, P. E., Lomas, M. R., Majkut, J., Metzl, N., … Woodward, F. I. (2009). Trends in the sources and sinks of carbon dioxide. *Nature Geoscience*, *2*(12), 831–836.

Liu, Q., Piao, S., Fu, Y. H., Gao, M., Peñuelas, J., & Janssens, I. A. (2019). Climatic warming increases spatial synchrony in spring vegetation phenology across the Northern Hemisphere. *Geophysical Research Letters*, *46*(3), 1641–1650.

Meng, L., Zhou, Y., Gu, L., Richardson, A. D., Peñuelas, J., Fu, Y., Wang, Y., Asrar, G. R., De Boeck, H. J., Mao, J., Zhang, Y., & Wang, Z. (2021). Photoperiod decelerates the advance of spring phenology of six deciduous tree species under climate warming. *Global Change Biology*, *27*(12), 2914–2927.

Menzel, A., Sparks, T. H., Estrella, N., Koch, E., Aasa, A., Ahas, R., Alm-Kübler, K., Bissolli, P., Braslavská, O., Briede, A., Chmielewski, F. M., Crepinsek, Z., Curnel, Y., Dahl, Å., Defila, C., Donnelly, A., Filella, Y., Jatczak, K., Måge, F., … Zust, A. (2006). European phenological response to climate change matches the warming pattern. *Global Change Biology*, *12*(10), 1969–1976.

Muñoz-Sabater, J., Dutra, E., Agustí-Panareda, A., Albergel, C., Arduini, G., Balsamo, G., Boussetta, S., Choulga, M., Harrigan, S., Hersbach, H., Martens, B., Miralles, D. G., Piles, M., Rodríguez-Fernández, N. J., Zsoter, E., Buontempo, C., & Thépaut, J.-N. (2021). ERA5-Land: A state-of-the-art global reanalysis dataset for land applications. *Earth System Science Data Discussions*, *13*(9), 4349–4383.

Myneni, R. B., Keeling, C., Tucker, C. J., Asrar, G., & Nemani, R. R. (1997). Increased plant growth in the northern high latitudes from 1981 to 1991. *Nature*, *386*(6626), 698–702.

Pastorello, G., Trotta, C., Canfora, E., Chu, H., Christianson, D., Cheah, Y.-W., Poindexter, C., Chen, J., Elbashandy, A., Humphrey, M., Isaac, P., Polidori, D., Reichstein, M., Ribeca, A., van Ingen, C., Vuichard, N., Zhang, L., Amiro, B., Ammann, C., … Papale, D. (2020). The FLUXNET2015 dataset and the ONEFlux processing pipeline for eddy covariance data. *Scientific Data*, *7*(1), 1–27.

Peaucelle, M., Janssens, I. A., Stocker, B. D., Ferrando, A. D., Fu, Y. H., Molowny-Horas, R., Ciais, P., & Peñuelas, J. (2019). Spatial variance of spring phenology in temperate deciduous forests is constrained by background climatic conditions. *Nature Communications*, *10*(1), 1–10.

Peñuelas, J., & Filella, I. (2001). Responses to a warming world. *Science*, *294*(5543), 793–795.

Peñuelas, J., & Filella, I. (2009). Phenology feedbacks on climate change. *Science*, *324*(5929), 887–888.

Piao, S., Liu, Q., Chen, A., Janssens, I. A., Fu, Y., Dai, J., Liu, L., Lian, X., Shen, M., & Zhu, X. (2019). Plant phenology and global climate change: Current progresses and challenges. *Global Change Biology*, *25*(6), 1922–1940. https://doi.org/10.1111/gcb.14619

Richardson, A. D., Andy Black, T., Ciais, P., Delbart, N., Friedl, M. A., Gobron, N., Hollinger, D. Y., Kutsch, W. L., Longdoz, B., Luyssaert, S., Migliavacca, M., Montagnani, L., Munger, J. W., Moors, E., Piao, S., Rebmann, C., Reichstein, M., Saigusa, N., Tomelleri, E., … Varlagin, A. (2010). Influence of spring and autumn phenological transitions on forest ecosystem productivity. *Philosophical Transactions of the Royal Society B: Biological Sciences*, *365*(1555), 3227–3246.

Richardson, A. D., Keenan, T. F., Migliavacca, M., Ryu, Y., Sonnentag, O., & Toomey, M. (2013). Climate change, phenology, and phenological control of vegetation feedbacks to the climate system. *Agricultural and Forest Meteorology*, *169*, 156–173. https://doi.org/10.1016/j.agrformet.2012.09.012

Sun, Y., Frankenberg, C., Wood, J. D., Schimel, D., Jung, M., Guanter, L., Drewry, D., Verma, M., Porcar-Castell, A., Griffis, T. J., Gu, L., Magney, T. S., Köhler, P., Evans, B., & Yuen, K. (2017). OCO-2 advances photosynthesis observation from space via solar-induced chlorophyll fluorescence. *Science*, *358*(6360), eaam5747.

Templ, B., Koch, E., Bolmgren, K., Ungersböck, M., Paul, A., Scheifinger, H., Busto, M., Chmielewski, F.-M., Hájková, L., Hodzić, S., Kaspar, F., Pietragalla, B., Romero-Fresneda, R., Tolvanen, A., Vučetič, V., Zimmermann, K., & Zust, A. (2018). Pan European Phenological database (PEP725): A single point of access for European data. *International Journal of Biometeorology*, *62*(6), 1109–1113.

Vitasse, Y., Signarbieux, C., & Fu, Y. H. (2018). Global warming leads to more uniform spring phenology across elevations. *Proceedings of the National Academy of Sciences of the United States of America*, *115*(5), 1004–1008.

Way, D. A., & Montgomery, R. A. (2015). Photoperiod constraints on tree phenology, performance and migration in a warming world. *Plant, Cell and Environment*, *38*(9), 1725–1736.

Yin, G., Verger, A., Filella, I., Descals, A., & Peñuelas, J. (2020). Divergent estimates of forest photosynthetic phenology using structural and physiological vegetation indices. *Geophysical Research Letters*, *47*(18), e2020GL089167.

Yuan, W., Zheng, Y., Piao, S., Ciais, P., Lombardozzi, D., Wang, Y., Ryu, Y., Chen, G., Dong, W., Hu, Z., Jain, A. K., Jiang, C., Kato, E., Li, S., Lienert, S., Liu, S., Nabel, J. E. M. S., Qin, Z., Quine, T., … Yang, S. (2019). Increased atmospheric vapor pressure deficit reduces global vegetation growth. *Science Advances*, *5*(8), eaax1396.

Zani, D., Crowther, T. W., Mo, L., Renner, S. S., & Zohner, C. M. (2020). Increased growing-season productivity drives earlier autumn leaf senescence in temperate trees. *Science*, *370*(6520), 1066–1071.

Zhang, Y., Commane, R., Zhou, S., Williams, A. P., & Gentine, P. (2020). Light limitation regulates the response of autumn terrestrial carbon uptake to warming. *Nature Climate Change*, *10*(8), 739–743.

Zhang, Y., Joiner, J., Alemohammad, S. H., Zhou, S., & Gentine, P. (2018). A global spatially contiguous solar-induced fluorescence (CSIF) dataset using neural networks. *Biogeosciences*, *15*(19), 5779–5800.

Zhang, Y., Parazoo, N. C., Williams, A. P., Zhou, S., & Gentine, P. (2020). Large and projected strengthening moisture limitation on end-of-season photosynthesis. *Proceedings of the National Academy of Sciences of the United States of America*, *117*(17), 9216–9222.

Zohner, C. M., Benito, B. M., Svenning, J.-C., & Renner, S. S. (2016). Day length unlikely to constrain climate-driven shifts in leaf-out times of northern woody plants. *Nature Climate Change*, *6*(12), 1120–1123.

SUPPORTING INFORMATION

Additional supporting information can be found online in the Supporting Information section at the end of this article.

How to cite this article: Descals, A., Verger, A., Yin, G., Filella, I., Fu, Y. H., Piao, S., Janssens, I. A., & Peñuelas, J. (2022). Radiation-constrained boundaries cause nonuniform responses of the carbon uptake phenology to climatic warming in the Northern Hemisphere. *Global Change Biology*, *00*, 1–12. https://doi.org/10.1111/gcb.16502